Supplementary Information

Superoxide Radical Derived Metal-Free Spiro-OMeTAD for Highly Stable Perovskite Solar Cells

Linfeng Ye[1,2,6], Jiahao Wu[1,2,6], Sergio Catalán-Gómez[3,6], Li Yuan[1,2], Riming Sun[1,2], Ruihao Chen[1,2], Zhe Liu[1,2], Jose María Ulloa[3], Adrian Hierro[3], Pengfei Guo[1,2,4*], Yuanyuan Zhou[5] & Hongqiang Wang[1,2*]

---

[1] State Key Laboratory of Solidification Processing, Center for Nano Energy Materials, School of Materials Science and Engineering, Northwestern Polytechnical University, Xi'an, 710071, China.

[2] Shaanxi Joint Laboratory of Graphene (NPU), Xi'an, 710071, China.

[3] ISOM, Universidad Politécnica de Madrid, 28040 Madrid, Spain.

[4] Research & Development Institute of Northwestern Polytechnical University in Shenzhen, Shenzhen, 518063, China.

[5] Department of Chemical and Biological Engineering, Hong Kong University of Science and Technology, Clear Water Bay, Hong Kong SAR, China.

[6] These authors contributed equally: Linfeng Ye, Jiahao Wu, Sergio Catalán-Gómez.

[*] Corresponding authors. Email: guopengfei@nwpu.edu.cn; hongqiang.wang@nwpu.edu.cn

Inventory of Supplementary Information

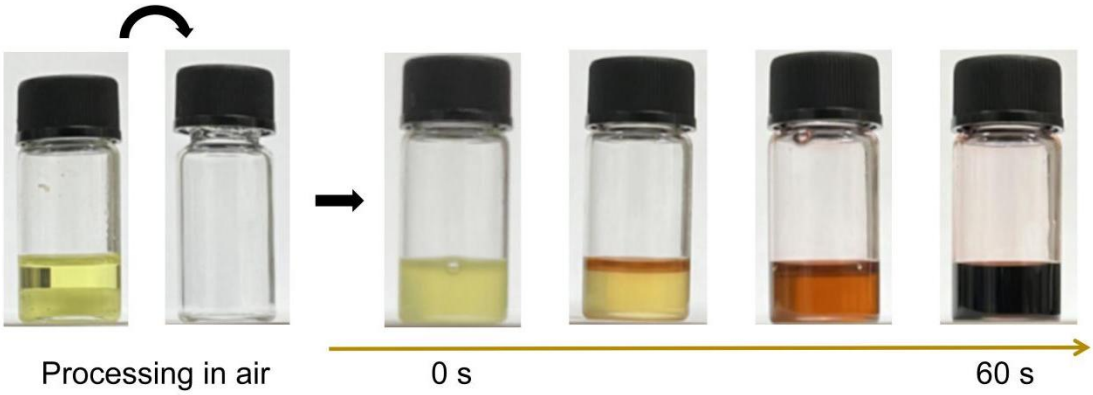

Supplementary Fig. 1. Optical evolution of the spiro-OMeTAD:$Eu(TFSI)_2$:CB solution in air. Detailed process is shown in Supplementary Movie 2 and Supplementary Movie 3.

Supplementary Note 1. EPR spectra and analyses

We performed the EPR spectra on spiro-OMeTAD:CB, spiro-OMeTAD:LiTFSI:CB, and spiro-OMeTAD:$Eu(TFSI)_2$:CB solutions to specifically detect the signal of $\bullet O_2^-$ in solutions with spiro-OMeTAD. After bubbling with O_2 for 10 s, we immediately detected the signal of $\bullet O_2^-$ and found the presence of $\bullet O_2^-$ in this solution based on the observation of its six peaks (Supplementary Fig. 2a). We would like to stress that, although spiro-$OMeTAD^+$ radicals are present at this stage, their amount is still relatively low compared to the $\bullet O_2^-$ (see the solution color in 10 s in Fig. 2a). Therefore, the EPR signals observed in this solution predominantly originate from the $\bullet O_2^-$.

We further performed the Electron Paramagnetic Resonance (EPR) spectra on spiro-OMeTAD:CB, spiro-OMeTAD:LiTFSI:CB, and spiro-OMeTAD:$Eu(TFSI)_2$:CB solutions to specifically detect the signal of spiro-$OMeTAD^+$ radicals in solutions. After bubbling with O_2 for 10 s, we did not immediately conduct the EPR test, but rather waited for 5 min before starting the test. The purpose of this delay was to allow sufficient oxidation of spiro-OMeTAD to generate spiro-$OMeTAD^+$ in solution. Therefore, the results in Supplementary Fig. 2b clearly demonstrate the EPR signal of spiro-$OMeTAD^+$ with one peak while no $\bullet O_2^-$ signal is observed. This indicates that, at this stage, the concentration of $\bullet O_2^-$ is significantly lower compared to spiro-$OMeTAD^+$ in the solutions.

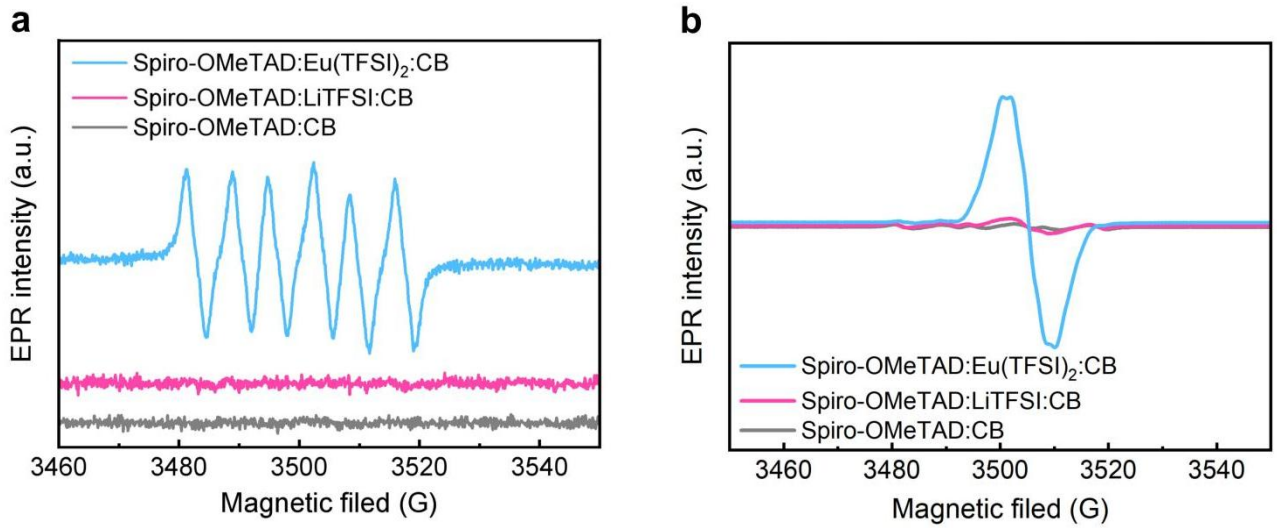

Supplementary Fig. 2. EPR spectra of different solutions. The spiro-OMeTAD:CB, spiro-OMeTAD:LiTFSI:CB and spiro-OMeTAD:Eu(TFSI)$_2$:CB solutions bubbled with O_2 for 10 s and tested immediately (**a**) and after 5 min (**b**).

Supplementary Note 2. Comparison of oxidation property between $\bullet O_2^-$ and O_2

Regarding the oxidation property comparison between $\bullet O_2^-$ and O_2, it should be noted that the superoxide radical ($\bullet O_2^-$) actually exhibits higher reactivity compared to molecular oxygen (O_2), primarily attributed to differences in their electronic structures. The $\bullet O_2^-$ is formed when one electron is individually stripped from an oxygen molecule, resulting in an unpaired electron. This unpaired electron gives the superoxide radical higher reactivity as it is more prone to engage in chemical reactions, such as electron transfer or redox reactions, with other substances including the spiro-OMeTAD. In contrast, molecular oxygen consists of two oxygen atoms sharing a pair of electrons, which contributes to its relative stability. To initiate a reaction with molecular oxygen, one must overcome its stability and the sharing of electron pairs, resulting in slower reaction rates. Therefore, the superoxide radical, with its unpaired electron characteristic, exhibits higher reactivity compared to molecular oxygen, which is consist with previous reports in other fields[1,2].

Experimentally, we further conducted the EPR spectra to compared the oxidation rate of $\bullet O_2^-$ and molecular oxygen in spiro-OMeTAD solutions (see Supplementary Fig. 2b). It is found that the $\bullet O_2^-$ strategy exhibits a higher oxidation peak than that of the conventional LiTFSI-doping. These results significantly demonstrate that $\bullet O_2^-$ shows an improved reaction rate compared with O_2 when involved in the in situ oxidation of spiro-OMeTAD in solution.

Supplementary Note 3. $\bullet O_2^-$ doping mechanism of spiro-OMeTAD solutions

We proposed the oxidation mechanism of $\bullet O_2^-$ for spiro-OMeTAD solutions, which can be described as follow: The lost electron from the Eu^{2+}-Eu^{3+} redox shuttle would first be recovered by O_2, contributing rapidly to the generation of the $\bullet O_2^-$. The resultant $\bullet O_2^-$ then oxidize the spiro-OMeTAD to a TFSI-stabilized spiro-OMeTAD$^+$ radical cation along with the Eu^{3+} reaction products. It should be noted that the conversion from O_2 to $\bullet O_2^-$ not O^{2-} in our present work is attributed to the imbalance in the involved amount between O_2 and Eu^{2+} (O_2 is excessive compared to Eu^{2+} when the concentration of $Eu(TFSI)_2$ is below 40 mol%), which could serve as a specific chemical condition[2]. Such chemical condition can limit interaction of O_2 with only one Eu^{2+} ion, resulting thus in the formation of $\bullet O_2^-$. However, the conversion from O_2 molecule to O^{2-} requires four electrons. In other words, for such conversion to occur, one oxygen molecule needs to interact with four Eu^{2+} ions simultaneously, leading to the difficulty of converting O_2 to O^{2-}. When the concentration of Eu^{2+} exceeds 40 mol% (e.g., >50 mol%), the spiro-OMeTAD solution exhibits a slower color change and a lighter final color during the bubbling with O_2 compared to the solution with a concentration of 40 mol% (see Supplementary Fig. 3), indicating that the amount of $\bullet O_2^-$ in solution decreases, subsequently reducing the oxidation of spiro-OMeTAD.

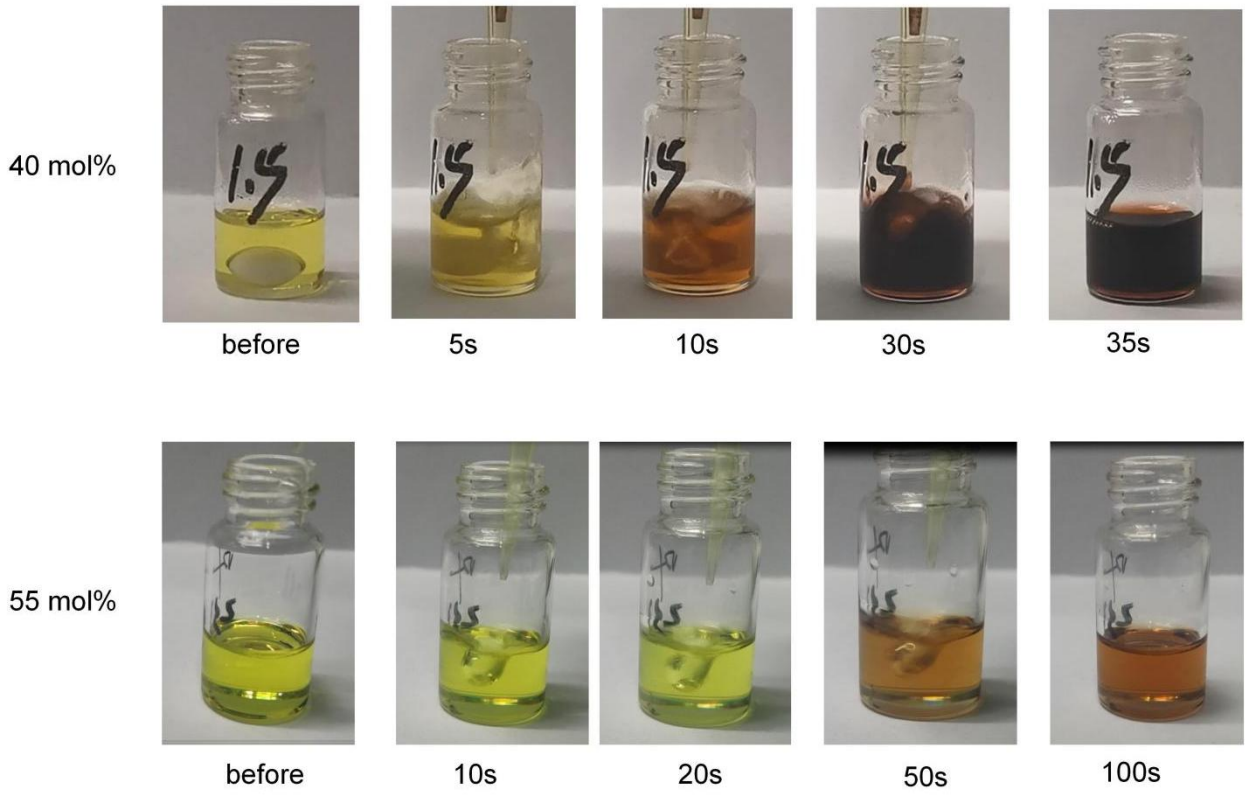

Supplementary Fig. 3. The color evolution of spiro-OMeTAD solutions with different concentrations of $Eu(TFSI)_2$ bubbled with O_2 over different time: 40 mol% (top) and 55 mol% (bottom).

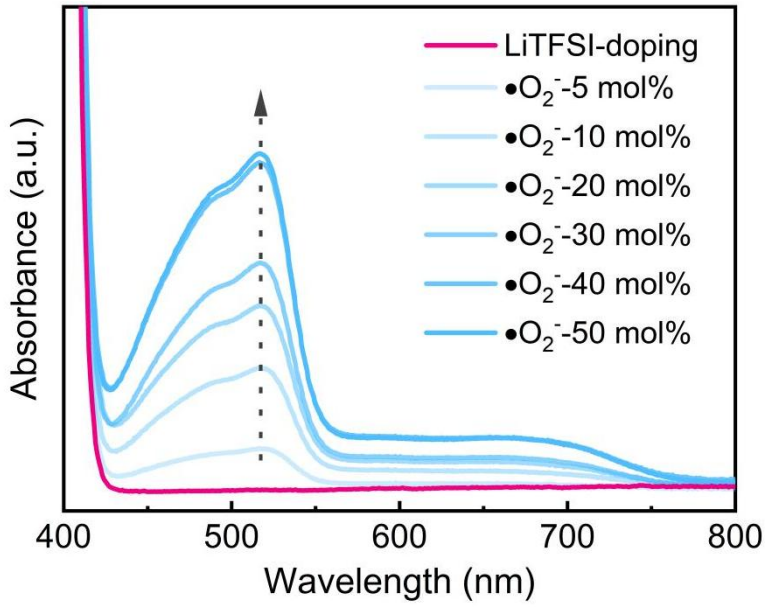

Supplementary Fig. 4. UV-vis spectra of the $\bullet O_2^-$-derived spiro-OMeTAD solution under different concentrations of $Eu(TFSI)_2$.

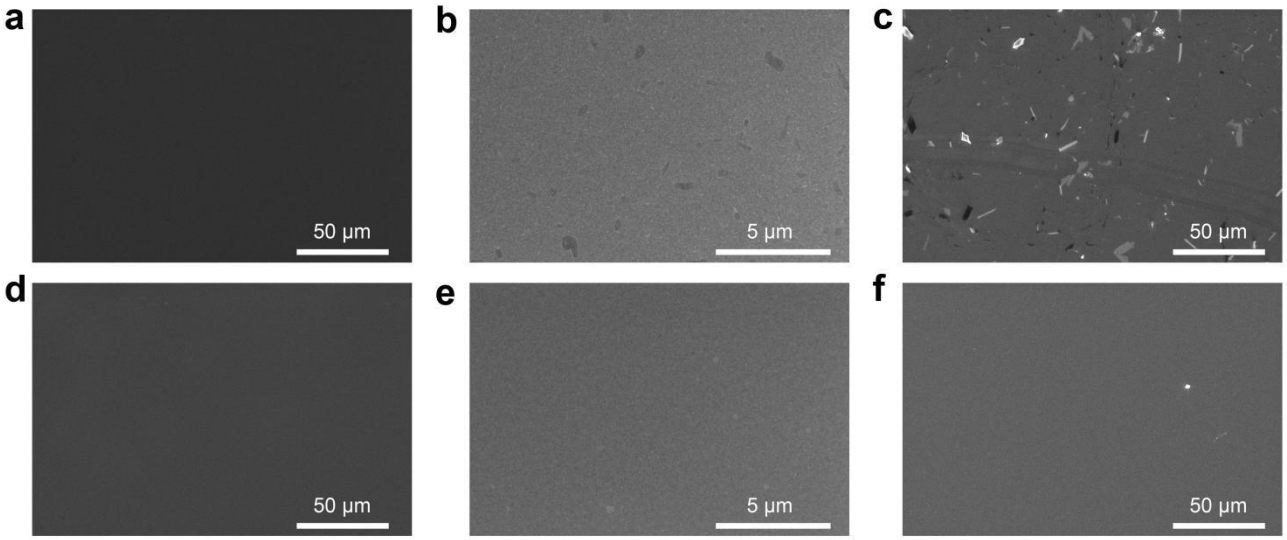

Supplementary Fig. 5. SEM images of different spiro-OMeTAD films. LiTFSI-doped spiro-OMeTAD before oxidation (**a**) and after oxidation of 12 h (**b**) and 10 months (**c**) in air, respectively. $\bullet O_2^-$-derived spiro-OMeTAD before (**d**) and after exposure of 12 h (**e**) and 10 months (**f**) in air, respectively.

Supplementary Note 4. Calculation for the hole mobility (μ) of different HTLs

We estimate the hole mobilities of the spiro-OMeTAD HTLs using the hole-only devices with a structure of FTO/PEDOT:PSS/spiro-OMeTAD/Au. The hole mobility (μ) of different HTLs was calculated using the space charge limit current (SCLC) model:

$$\mu = \frac{8JL^3}{9\varepsilon\varepsilon_0(V-V_r-V_{bi})^2} \quad (1)$$

where J is the current density; L is the thickness of HTLs; ε_0 and ε are the vacuum permittivity and the dielectric permittivity, respectively. V is the applied voltage, V_r is the voltage loss resulting from radiative recombination, and V_{bi} is the built-in potential. The hole mobilities were accordingly calculated to be 3.63×10^{-4}, 5.69×10^{-4}, 9.79×10^{-4}, 1.01×10^{-3} and 7.43×10^{-4} cm^2 V^{-1} s^{-1} for the LITFSI-doped HTL, 10 mol%, 20 mol%, 40 mol%, and 50 mol% $\bullet O_2^-$-derived HTLs (Supplementary Fig. 6), respectively.

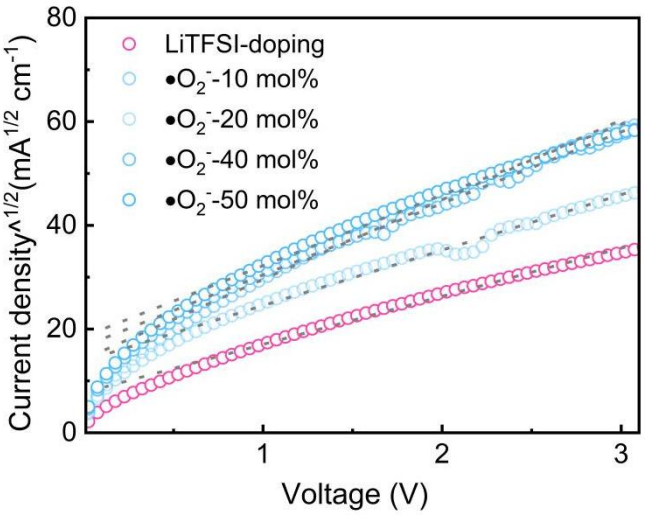

Supplementary Fig. 6. Hole mobilities of different HTLs based on LiTFSI- and $\bullet O_2^-$-derived spiro-OMeTAD using the SCLC mode.

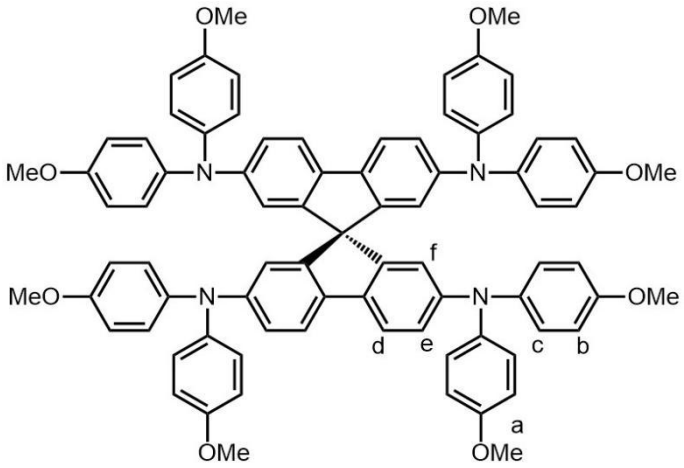

Supplementary Fig. 7. The molecular structure of spiro-OMeTAD.

Supplementary Note 5. Analyses for $\bullet O_2^-$-doping saturation in spiro-OMeTAD solutions

Previous studies have indicated that the dopants do not achieve a doping efficiency of over 100%[3,4]. Instead, the doping efficiency is closer to less than 20%. This highlights that only a fraction of spiro-OMeTAD (~8 mol %) is oxidized by the addition of dopants (e.g., LiTFSI) up to a concentration of 50 mol%. This can be attributed to doping saturation, which is consistent with previous reports in other organic semiconductor systems and arises due to the increase in energetic disorder induced by long-range Coulomb interactions when increasing the number of dopants[5,6].

Regarding the determination of doping saturation in the 40 mol% in the present work, we conducted a series of characterizations, including UV-vis spectra, conductivity/mobility tests, and PCE optimization (see Fig. 2f, Fig. 3b, Fig. 4 a-c, Supplementary Fig. 4, Supplementary Fig. 6, and Supplementary Table 3). In brief, both the polaron absorption peak centered at about 521 nm and the conductivity/hole mobility of the $\bullet O_2^-$-derived spiro-OMeTAD with the doping concentration up to 40 mol% reached peak values. Upon further increasing the concentration of $Eu(TFSI)_2$ (e.g., 50 mol%), all corresponding parameters showed either no change or a decrease. Moreover, higher concentrations of $Eu(TFSI)_2$ exceeding 40 mol% are not beneficial to the photovoltaic performance of PSCs (Supplementary Table 3). This could be due to the high concentration of $Eu(TFSI)_2$ reducing the amount of $\bullet O_2^-$ in solution and subsequently reducing the oxidation of spiro-OMeTAD (Supplementary Fig. 3). These results demonstrated that the doping of spiro-OMeTAD in solution reached saturation at the concentration up to 40 mol% of $Eu(TFSI)_2$ to spiro-OMeTAD.

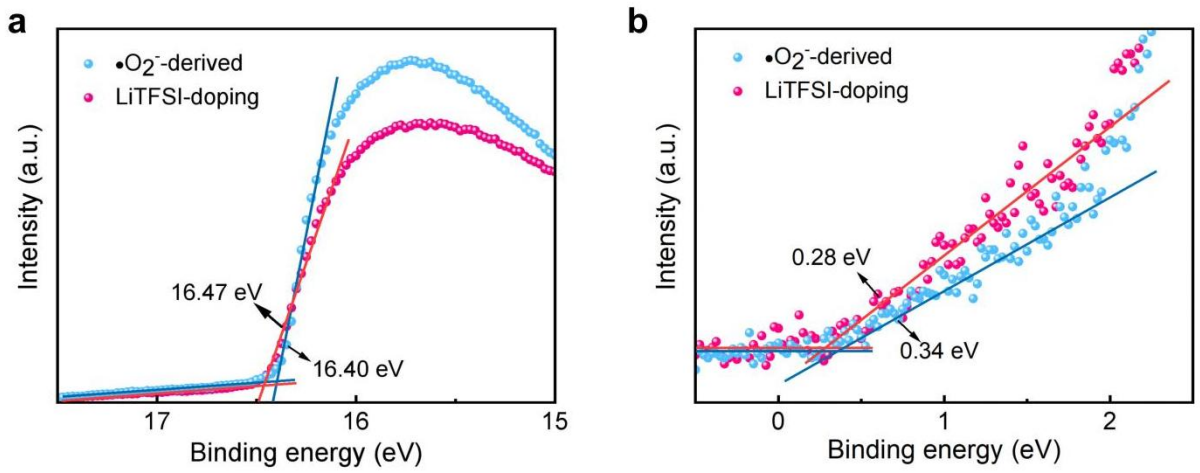

Supplementary Fig. 8. Ultraviolet photoelectron spectroscopy (UPS) spectra of different spiro-OMeTAD HTLs. **a** Secondary electron cut-off region. **b** Valence band region.

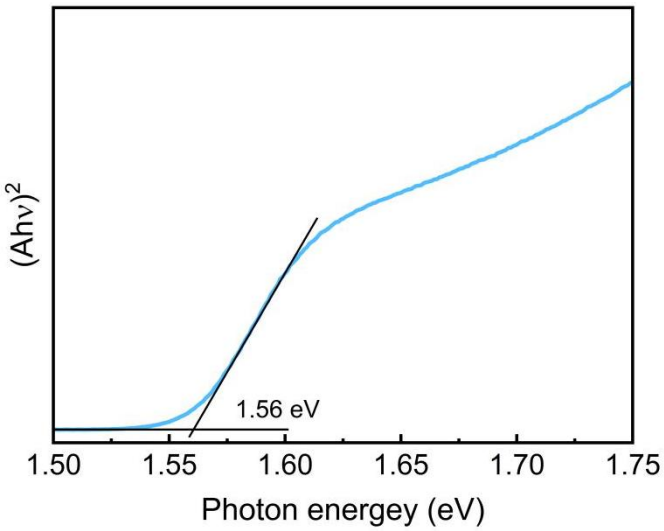

Supplementary Fig. 9. The Tauc plot of the $Cs_{0.05}FA_{0.85}MA_{0.10}PbI_{2.91}Br_{0.09}$ perovskite film.

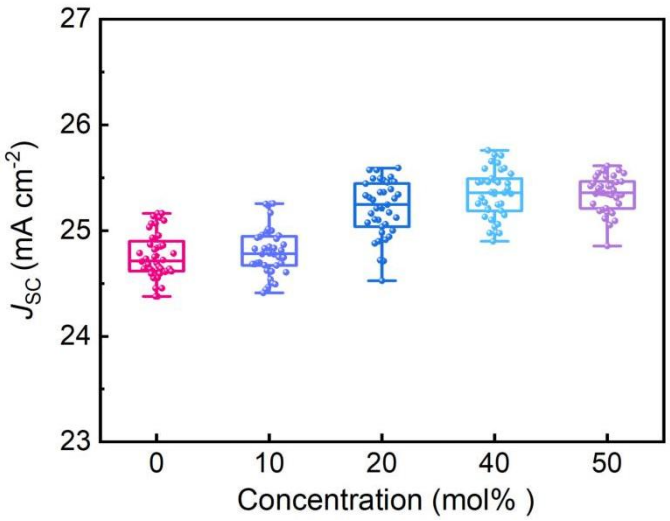

Supplementary Fig. 10. Statistical distribution of 40 individual CsFAMA devices with different •O_2^--derived spiro-OMeTAD HTLs for J_{SC}.

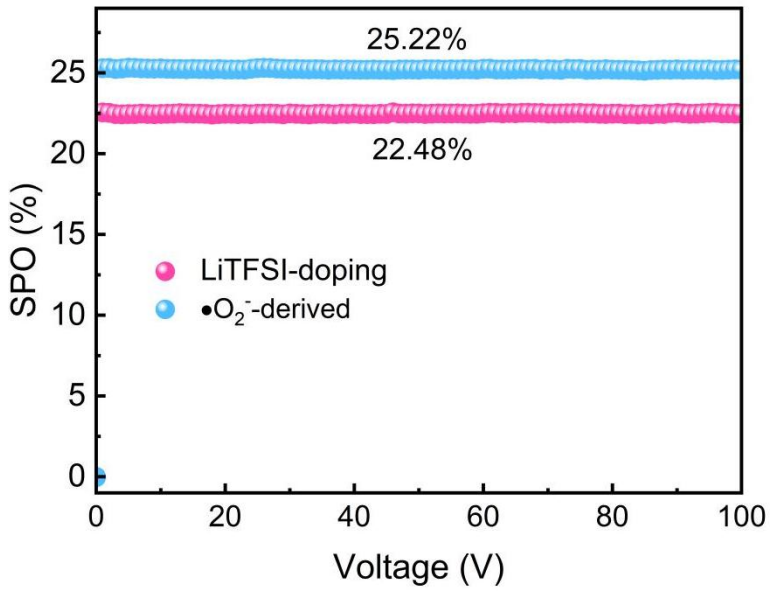

Supplementary Fig. 11. Stabilized power output (SPO) of the champion CsFAMA devices with LiTFSI-doped and $\bullet O_2^-$-derived spiro-OMeTAD HTLs.

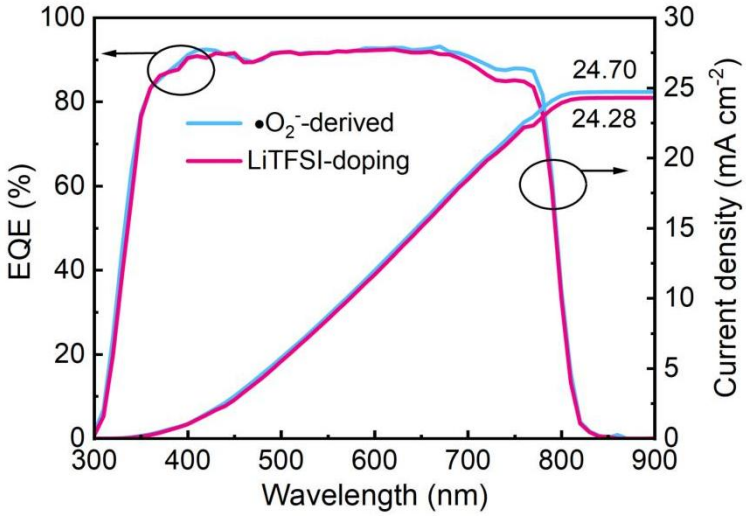

Supplementary Fig. 12. EQE and integrated current density curves for the champion CsFAMA devices with LiTFSI-doped and •O_2^--derived spiro-OMeTAD HTLs.

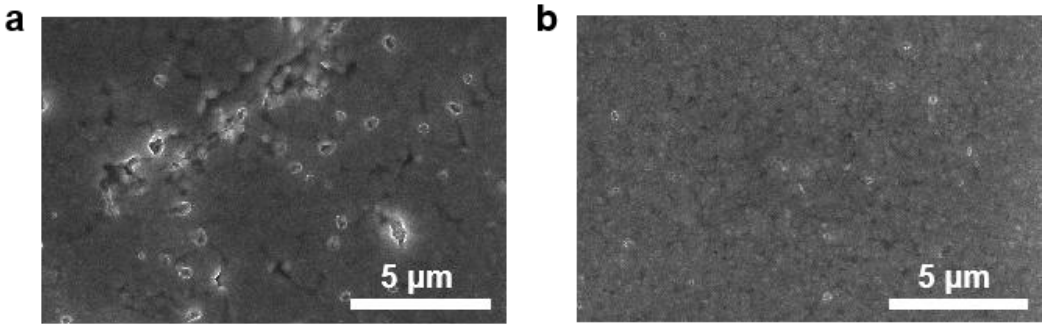

Supplementary Fig. 13. SEM images of different spiro-OMeTAD deposited on perovskite films after aging in double 85 condition (85% RH and 85°C) for 40 min. **a** LiTFSI-doped spiro-OMeTAD. **b** •O_2^--derived spiro-OMeTAD.

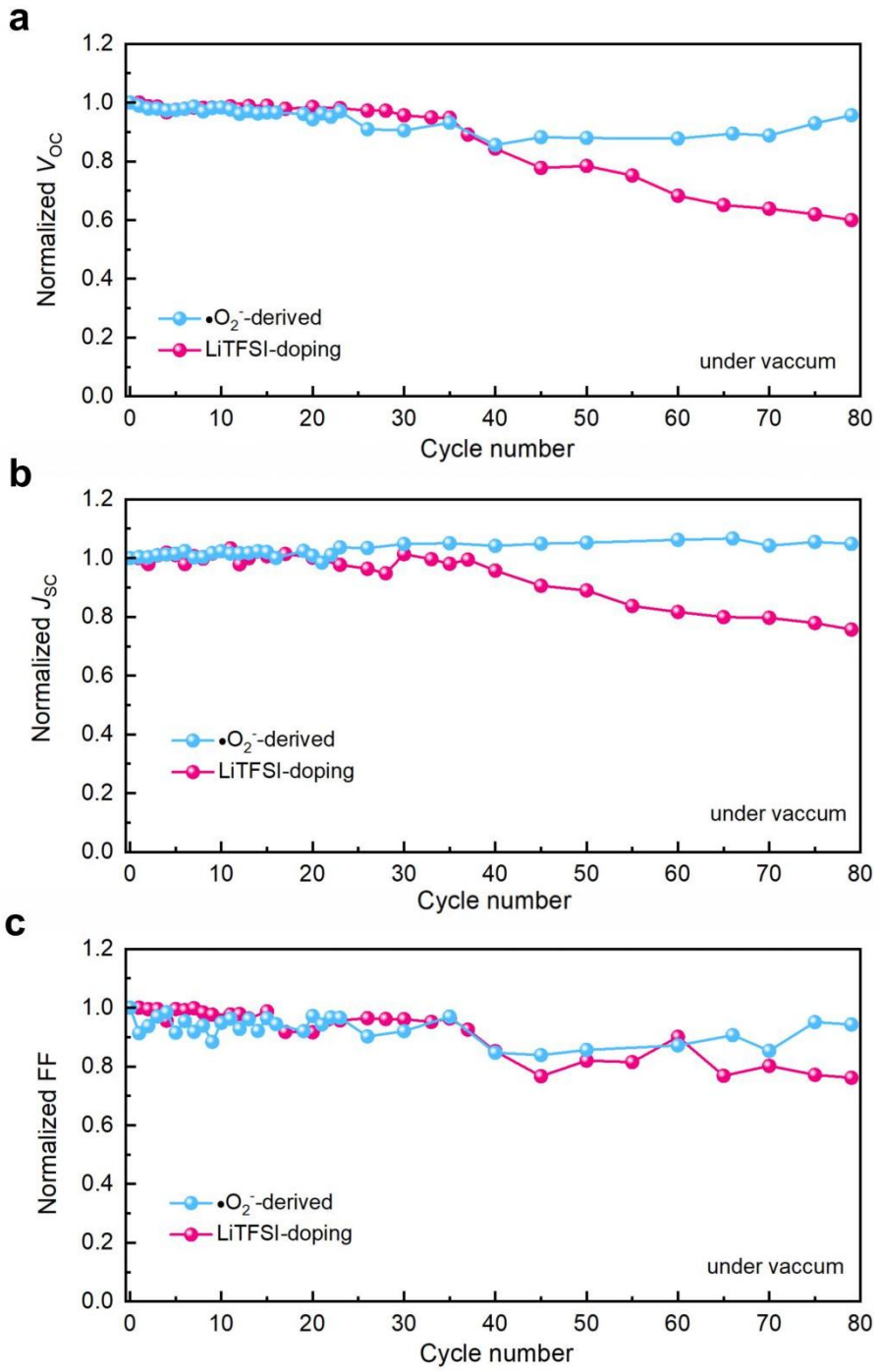

Supplementary Fig. 14. Light-thermal cycling stability of CsFAMA PSCs with different HTLs under simulated LEO conditions. The evolution of photovoltaic parameters at V_{OC} (**a**), J_{SC} (**b**), and FF (**c**).

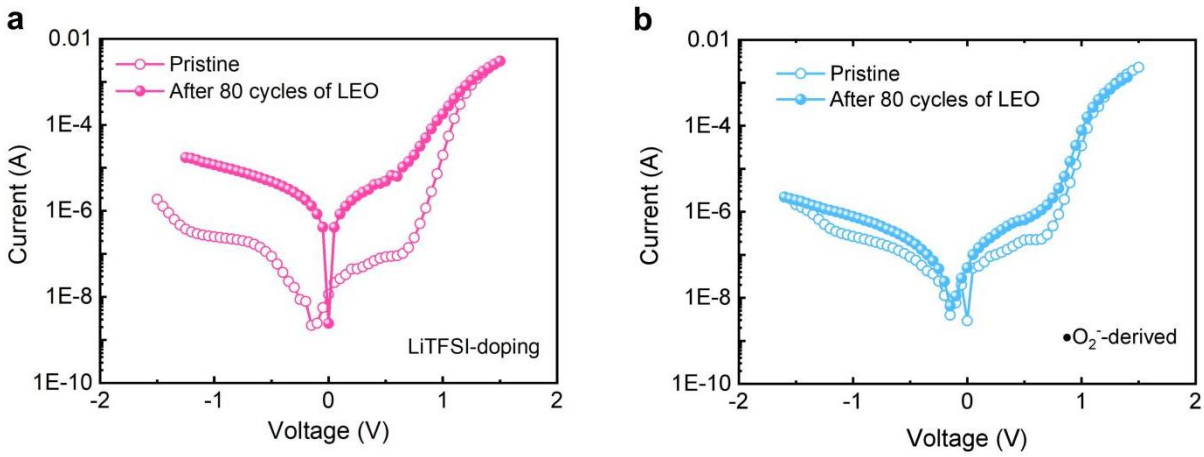

Supplementary Fig. 15. Dark *J-V* curves of PSCs with different HTLs before and after LEO cycles. **a** LiTFSI-doped spiro-OMeTAD. **b** $\bullet O_2^-$-derived spiro-OMeTAD.

Supplementary Note 6. The effect of environmental factors on the $\bullet O_2^-$-doping rate

For the conventional post-oxidation of LiTFSI-doped spiro-OMeTAD HTLs, the environmental factors such as temperature and humidity indeed affect the degree of oxidation of spiro-OMeTAD and the repeatability of devices. However, for the oxidation of spiro-OMeTAD solutions by $\bullet O_2^-$, we actually presented two recipes in the present work, including pumping O_2 into the spiro-OMeTAD solution in air and exposing the spiro-OMeTAD solution to air (see Supplementary Movie 1, Supplementary Movie 2, and Supplementary Movie 3). These routes actually involved the oxidation of spiro-OMeTAD in solution under different humidity conditions. The route I of pumping O_2 was conducted in ambient atmosphere with a relative humidity (RH) of 40%-70%, Supplementary Movie 1). While the route II of exposing the spiro-OMeTAD solution was carried out either in the ambient atmosphere or in an air glovebox (RH of ~10%, Supplementary Movie 2 and Supplementary Movie 3). It appears that the humidity condition did not affect the device performance (see Supplementary Fig. 16, the device was prepared by re-dissolving the spiro-OMeTAD powder from route II) when compared to route I (Fig. 4a-c). We did not highlight the variate in humidity in the present work owing to the remarkable repeatability of the obtained devices regardless of the environmental humidity. More importantly, the absence of hygroscopic LiTFSI in spiro-OMeTAD solution, along with the ultrafast oxidation process in air (30 s), could contribute to minimizing the impact of the external environment.

Regarding the effect of temperature on the degree of oxidation of spiro-OMeTAD in solution, it is well known that properties such as viscosity, O_2 diffusion coefficient, solubility, and individual ion diffusion coefficients can change with different temperatures, and play a primary role in the generation of $\bullet O_2^-$ and its stability[2]. An increase in temperature can also influence the reactivity of $\bullet O_2^-$ and spiro-OMeTAD, thereby affecting the rate of oxidation of spiro-OMeTAD. Experimentally, we further conducted the experiments by pumping O_2 in spiro-OMeTAD:$Eu(TFSI)_2$ solutions at different temperatures (0°C, 23°C, 40°C, 60°C and 85°C). It was observed that the oxidation rate of the spiro-OMeTAD solution gradually increased with higher temperatures. However, over a sufficient period of time, the degree of oxidation reached consistent levels (see the final color at 40°C, 60°C and 85°C in Supplementary Movie 4 and Supplementary Fig. 17, respectively), indicating the amount of formed $\bullet O_2^-$ at different temperatures is identical. These results suggest that the final amount of formed $\bullet O_2^-$ is predominantly influenced by the concentration of $Eu(TFSI)_2$ introduced and the duration of oxygen exposure. Therefore, it is expected that the doping of

spiro-OMeTAD HTLs and the performance of their devices would not be affected by the applied temperatures. For confirming this point, we have also supplemented photovoltaic performance of PSCs based on the $\bullet O_2^-$-derived spiro-OMeTAD HTLs under different temperatures (see Supplementary Fig. 18). These results show that devices based on $\bullet O_2^-$-derived spiro-OMeTAD HTLs prepared at 0°C, 23°C, 60°C and 85°C deliver average PCEs of 24.56%, 24.70%, 24.60%, and 24.70%, respectively, demonstrating almost consistent photovoltaic performance.

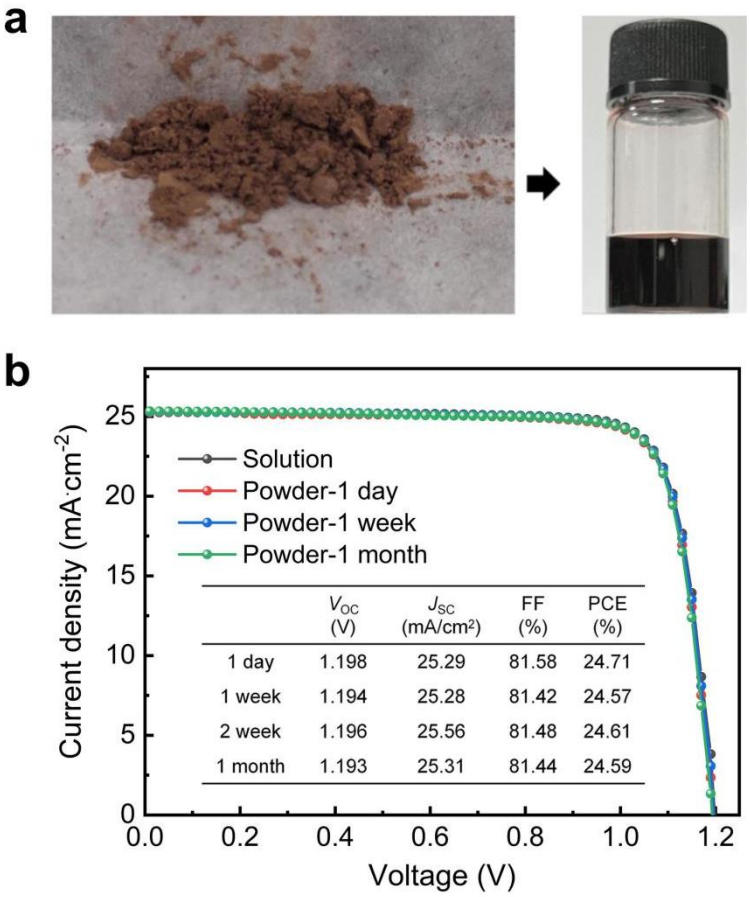

Supplementary Fig. 16. PSCs using $\bullet O_2^-$-derived spiro-OMeTAD powder as HTLs. **a** Optical photographs of $\bullet O_2^-$-derived spiro-OMeTAD powder and its further dissolution in CB solvent. **b** *J-V* curves of PSCs using the powder with various storage times. It is worth noting that the $\bullet O_2^-$-derived spiro-OMeTAD powder can be directly dissolved in CB solvent and used to deposit the HTL of PSCs without any post-treatment.The obtained PCE employing resulted powders with 1 month aging still can match those of devices using fresh spiro-OMeTAD solutions or powders.

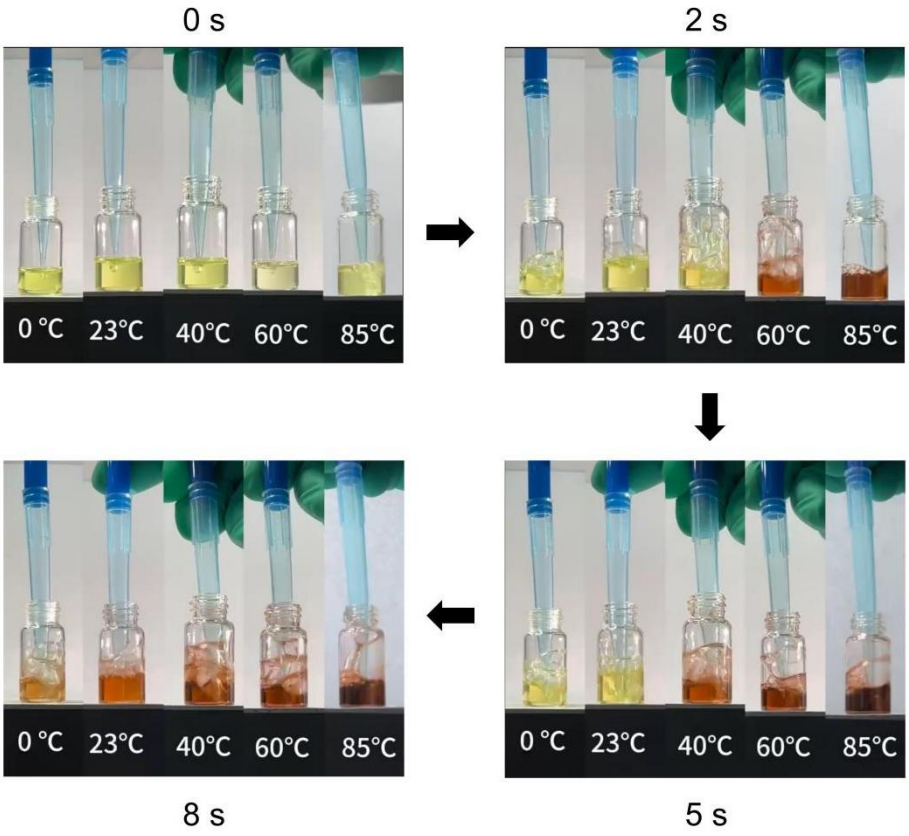

Supplementary Fig. 17. The color evolution of spiro-OMeTAD:Eu(TFSI)$_2$ solutions bubbled with O_2 at different temperature.

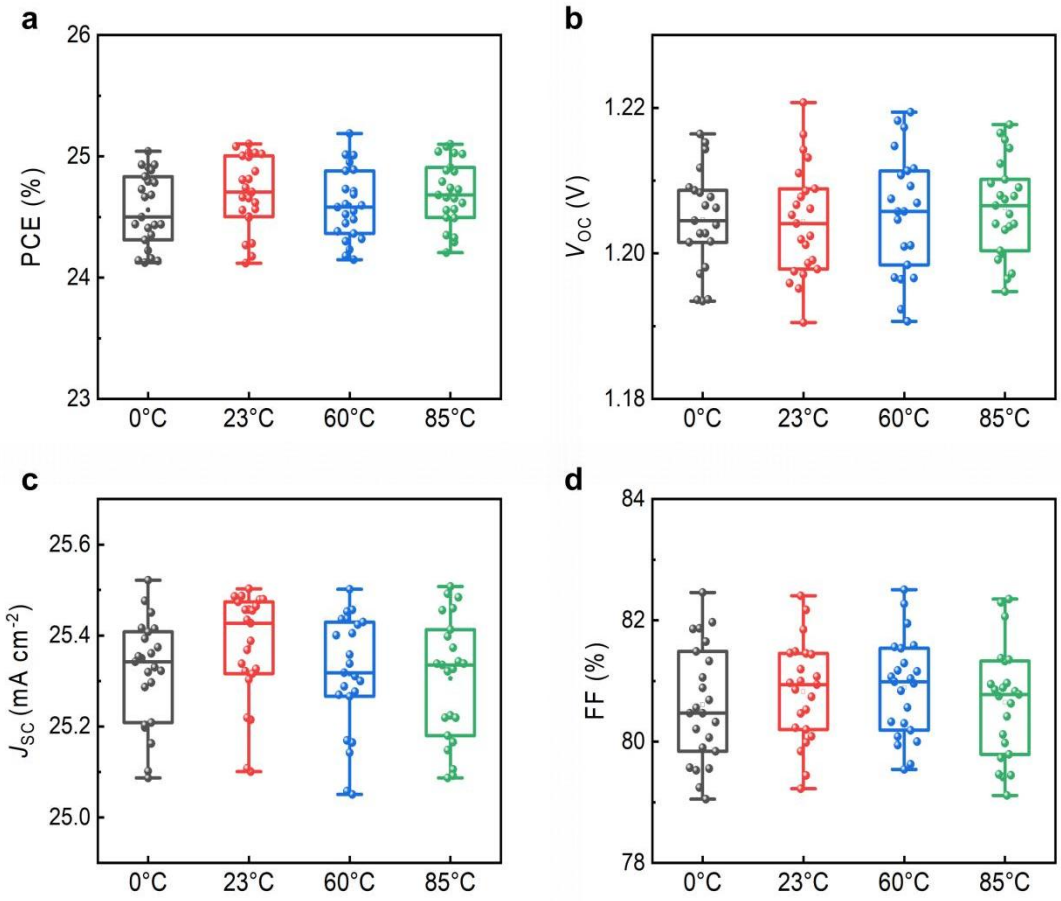

Supplementary Fig. 18. Statistical distribution of 25 individual PSC devices based on $\bullet O_2^-$-derived spiro-OMeTAD HTLs prepared at different temperatures. **a** PCE. **b** V_{OC}. **c** J_{SC}. **d** FF. The employed concentration of $Eu(TFSI)_2$ for all devices is 40 mol%.

Supplementary Note 7. The advantages of the $\bullet O_2^-$ strategy compared to previous works

Regarding the advantages of the $\bullet O_2^-$ strategy, the present work clearly distinguishes from the reported works on doping process of spiro-OMeTAD HTLs, and shows obvious advantages in the following two aspects: **(1) Metal-free spiro-OMeTAD HTLs.** Different from the literature that involves bubbling a spiro-OMeTAD:LiTFSI solution with CO_2/O_2 under ultraviolet light illumination[7], we employ in present work a variant-valence $Eu(TFSI)_2$ salt that could generate $\bullet O_2^-$ in air for facile and adequate oxidation of spiro-OMeTAD in solution within 30 s, without necessitating the adding of LiTFSI and UV light irradiation. Thus, the $\bullet O_2^-$-derived Li-free (even metal-free) spiro-OMeTAD HTLs possess notable advantages, especially in terms of environmental stability. **(2) Fast synthetic route.** Different from the literature that involves additional ionic salts to modulate the work function of spiro-OMeTAD HTLs[6], we employ in present work only a variant-valence $Eu(TFSI)_2$ salt that could generate $\bullet O_2^-$ in air for facile and adequate oxidation of spiro-OMeTAD in solution within 30 s, obtaining instantly high conductivity and ideal work function, as well as high PCEs of >25% that can rival the efficiency of devices based on the co-regulated spiro-OMeTAD HTLs. It should be noted that both the organic radical and ionic salt process need be subjected to a complicated and tedious wet-chemical synthetic procedure, including solvent exchange, filtration, drying, recrystallization, purification, working under reduced pressure/low temperature/inert atmosphere, and more. Completing the entire route for doping spiro-OMeTAD HTLs using these methods typically takes several days. In addition, we have actually presented two synthetic routes in our work, including pumping O_2 into the spiro-OMeTAD solution and exposing the spiro-OMeTAD solution to air. (see Supplementary Movie 1, Supplementary Movie 2, and Supplementary Movie 3). Given that the amount of oxygen involved and the time spent of less than 30 s in the entire synthesis process, we believe that the corresponding preparation cost is negligible, especially for the second route.

Supplementary Table 1. Reported PCE and long-term stability of PSCs based on modified spiro-OMeTAD HTLs.

Addictive	Device and Perovskite	PCE [%]	Stability	Ref.
Spiro-OMeTAD$^{2\bullet+}$(TFSI$^-$)$_2$ and TBMP$^+$TFSI$^-$	$(FAPbI_3)_{0.99}(MAPbBr_3)_{0.01}$	25.1*	The T_{80} of PSCs (unencapsulated) from ~96 to ~1240 hours under high RH of ~70 ± 5% and T_{80} from ~264 to ~796 hours under ~70 ± 3°C	6
Spiro-OMeTAD(TFSI)$_2$	$Rb_{0.05}Cs_{0.05}FA_{0.8}MA_{0.07}PbBr_{0.4}I_{2.57}$	19.3	65% of the initial performance after 300 h in comparison to 40% for the control device under continuous illumination at 1 sun, 50°C and 40% relative humidity	8
TBA-PF_6	$Rb_{0.05}Cs_{0.05}FA_{0.8}MA_{0.07}PbBr_{0.4}I_{2.57}$	17.4	Maintaining more than 60% of the initial efficiency after 1 month of aging in the dark with 50% humidity and after 8 h of heating at 85°C in ambient conditions (50% humidity)	9
1-butyl-3-methylpyridinium bis(trifluoromethylsulfonyl)imide (BMPyTFSI)	$((FAPbI_3)_{0.85}(MAPbBr_3)_{0.15})$	14.0	-	10
M(TFSI)n dopants where M = Zn^{2+}, Ca^{2+}, Cu^{2+}, and Sc^{3+}; n = 1, 2, 3	$Cs_{0.05}FA_{0.85}MA_{0.1}Pb(I_{0.9}Br_{0.1})_3$	22.0	-	11
NaTFSI	$(FAPbI_3)_{0.95}(MAPbBr_3)_{0.05}$	22.4	Maintaining >80% of the initial performance after 500 h of continuous 1 sun illumination under MPP at 45°C	12
Zn(TFSI)$_2$	$Cs_{0.05}FA_{0.81}MA_{0.14}PbI_{2.55}Br_{0.45}$	21.5	Resulting in a 21% decrease in the PCE after 100 h aging at MPP under full sun	13
MgTFSI$_2$ and CaTFSI$_2$	$Cs_{0.05}FA_{0.81}MA_{0.14}PbI_{2.55}Br_{0.45}$	18.9	Maintaining 83% its initial efficiency for 193 days after aging in ambient air (RH% = 55-70%)	14
Fe(F20TPP)Cl	$(FAPbI_3)_{0.95}(MAPbBr_3)_{0.05}$	21.5	Retaining 84% of its initial efficiency after 900 h under continuous one sun illumination and 89% of its initial efficiency after 50 days in an ambient air	15
LiPFSI	$(FAPbI_3)_{0.875}(MAPbBr_3)_{0.075}(CsPbI_3)_{0.05}(PbI_2)_{0.03}$	22.1	-	16
CO_2 +LiTFSI+TBP	$Cs_{0.05}FA_{0.81}MA_{0.14}PbI_{2.55}Br_{0.45}$	19.1	Maintaining 80% of its initial maximum power even after 500 h of MPP tracking	7

$FeCl_3$+LiTFSI+TBP	$Cs_{0.05}FA_{0.81}MA_{0.14}PbI_{2.55}Br_{0.45}$	17.2	-	[17]
Co(III)-grafted ultrathin graphitic carbon nitride+LiTFSI+TBP	Cs0.05MA0.1FA0.85Pb(I0.97 Br0.03)3	23.0	Maintain 88 % and 80 % of initial PCE after exposure to the ambient air for 1200 h and 85 ℃ for 720 h	[18]
V_2O_5+LiTFSI+TBP	$Cs_{0.05}FA_{0.81}MA_{0.14}PbI_{2.55}Br_{0.45}$	20.5	Retaining 90% of the initial efficiency after exposure to ambient air with a humidity of 40% for 30 days	[19]
1-dodecanethiol+LiTFSI+ TBP	$Cs_{0.05}FA_xMA_{1-x}PbI_3$	23.1	Retaining 90% of peak performance under continuous illumination for 1000 h	[20]
1,6-diazidohexane	$FA_{0.92}MA_{0.08}PbI_3$	22.7	Maintaining 91% under open-circuit condition with continuous light illumination, after aging for 900 h.	[21]
Cobalt (III) trifluoride (CoF_3) +LiTFSI+TBP	$FA_{1-x}MA_xPbI_3$	23.0	Maintains 90% of the initial PCE after being aged in dry air for 3500 h Maintaining 91% of its initial PCE after one month of storage in the atmosphere with 20-30% relative humidity	[22]
3-Chloroperoxybenzoic acid+LiTFSI+TBP	$FA_{0.95}MA_{0.05}PbI_{2.85}Br_{0.15}$	23.3	Maintaining 82 % of the initial PCE in ambient atmosphere (room temperature and relative humidity ~ 30 %) in dark for 32 days	[23]
$K_3[Fe(CN)_6]$ +LiTFSI+TBP	$Cs_{0.05}FA_{0.81}MA_{0.14}PbI_{2.55}Br_{0.45}$	20.8	Maintaining 65.6% of its initial PCE after 16 days of storage	[24]
12-crown-4+LiTFSI	$Cs_{0.05}FA_{0.81}MA_{0.14}PbI_{2.55}Br_{0.45}$	21.0	Maintains 87% of the initial PCE even after 60 days exposure in air	[25]
Benzoyl peroxide +LiTFSI+TBP	$MAPbI_3$	16.8	-	[26]
12-Crown-4+LiTFSI	$Cs_{0.05}FA_{0.85}MA_{0.1}Pb(I_{0.97}Br_{0.03})_3$	23.2	Retaining 95.9% of the initial PCE after aging over 2400 h in the dark at 25°C and 30-50%. Keep 81.6% of the initial PCE after thermal aging over 450 h in N_2	[27]
Silicon dioxide particles	$Cs_{0.1}(FA_{0.92}MA_{0.08})_{0.9}Pb(I_{0.9}Br_{0.04}Cl_{0.06})_3$	22.3	Maintaining 91 and 95% of initial efficiency after thermal aging at 85°C for 1126 h and SPO operation for 1235 h in a nitrogen atmosphere	[28]
$KMnO_4$	$Cs_{0.05}(MA_{0.17}FA_{0.83})_{0.95}Pb(I_{0.83}Br_{0.17})_3$	20.0	-	[29]
IP-TFSI	$FAPbI_3$	25.16 (24.85*)	Maintaining 94% its initial efficiency for 2072h after aging in ambient air (RH = 30%) 90% of its initial maximum power even after 1370 h of MPP tracking	[30]

			Maintain 90% of initial PCE after exposure 85℃ for 1000 h in N_2.	
$Eu(TFSI)_2$ induced $•O_2^-$	$Cs_{0.05}FA_{0.85}MA_{0.10}PbI_{2.91}Br_{0.09}$	25.45% (active area 0.05 cm^2)	Maintaining over 80% of their initial efficiency after 5000 h in ambient air under RH of 70%, over 90% of their initial PCEs after annealing at 85°C for 1000 h, over 90% of their initial efficiency after 1000 h of operation at the maximum power point and after 80 light-thermal cycles under simulated low earth orbit condition	This work
		20.76% (active area 18 cm^2)	-	

* Certified PCE.

Supplementary Table 2. Summaries of fitting parameters for TRPL spectra with a structure of FTO/CsFAMA/different spiro-OMeTAD.

Samples	A_1	τ_1 (ns)	A_2	τ_2 (ns)	τ_{ave} (ns)
CsFAMA/LiTFSI-doping-HTL	0.25	3.6	0.75	78.6	77.5
CsFAMA/$\bullet O_2^-$-derived -HTL	0.85	2	0.15	29.5	21.9

Supplementary Table 3. Statistical photovoltaic parameters of PSCs based on different spiro-OMeTAD HTLs.

Devices	Average V_{OC} (V)	Average J_{SC} (mA cm^{-2})	Average FF (%)	Average PCE (%)
LiTFSI-doping	1.161 ± 0.006	24.77 ± 0.22	77.89 ± 0.37	22.40 ± 0.31
•O_2^--10 mol%	1.173 ± 0.005	24.80 ± 0.23	79.28 ± 0.36	23.06 ± 0.25
•O_2^--20 mol%	1.185 ± 0.005	25.21 ± 0.27	80.77 ± 0.45	24.13 ± 0.19
•O_2^--40 mol%	1.205 ± 0.004	25.36 ± 0.23	82.01± 0.44	25.06 ± 0.25
•O_2^--50 mol%	1.195 ± 0.005	25.36 ± 0.17	81.30 ± 0.45	24.54 ± 0.29

Supplementary Table 4. Statistical photovoltaic parameters of PSCs based on $\bullet O_2^-$-derived spiro-OMeTAD HTLs prepared at different temperatures.

Devices	Average V_{OC} (V)	Average J_{SC} (mA cm^{-2})	Average FF (%)	Average PCE (%)
0°C	1.205 ± 0.007	25.32 ± 0.11	80.61 ± 0.96	24.56 ± 0.30
23°C	1.204 ± 0.008	25.37 ± 0.12	80.83 ± 0.82	24.70 ± 0.30
60°C	1.206 ± 0.008	25.32 ± 0.13	80.89 ± 0.81	24.60 ± 0.29
85°C	1.206 ± 0.006	25.31 ± 0.13	80.65 ± 0.92	24.70 ± 0.27

Note: The employed concentration of $Eu(TFSI)_2$ for all devices is 40 mol%.

Supplementary References

1. Xiao, X. et al. A unique Fe-N_4 coordination system enabling transformation of oxygen into superoxide for photocatalytic C-H activation with high efficiency and selectivity. *Adv. Mater.* **34**, 2200612 (2022).
2. Hayyan, M., Hashim, M. A. & AlNashef, I. M. Superoxide ion: generation and chemical implications. *Chem. Rev.* **116**, 3029-3085 (2016).
3. Forward, R. L., Chen, K. Y., Weekes, D. M., Dvorak, D. J., Cao, Y. & Berlinguette, C. P. Protocol for quantifying the doping of organic hole-transport materials. *ACS Energy Lett*. **4**, 2547-2551 (2019).
4. Schölin, R., Karlsson, M. H., Eriksson, S. K., Siegbahn, H., Johansson, E. M. J. & Rensmo, H. Energy level shifts in spiro-OMeTAD molecular thin films when adding Li-TFSI. *J. Phys. Chem. C* **116**, 26300-26305 (2012).
5. Tietze, M. L., Pahner, P., Schmidt, K., Leo, K. & Lüssem, B. Doped organic semiconductors: trap-filling, impurity saturation, and reserve regimes. *Adv. Funct. Mater*. **25**, 2701-2707 (2015).
6. Zhang, T. et al. Ion-modulated radical doping of Spiro-OMeTAD for more efficient and stable perovskite solar cells. *Science* **377**, 495-501 (2022).
7. Kong, J. et al. CO_2 doping of organic interlayers for perovskite solar cells. *Nature* **594**, 51-56 (2021).
8. Tan, B. et al. LiTFSI-free Spiro-OMeTAD-based perovskite solar cells with power conversion efficiencies exceeding 19%. *Adv. Energy Mater.* **9**, 1901519 (2019).
9. Zhang, J., Zhang, T., Jiang, L., Bach, U. & Cheng, Y. 4-tert-butylpyridine free hole transport materials for efficient perovskite solar cells: A new strategy to enhance the environmental

and thermal stability. *ACS Energy Lett.* **3**, 1677-1682 (2018).

10. Caliò, L., Salado, M., Kazim, S. & Ahmad, S. A generic route of hydrophobic doping in hole transporting material to increase longevity of perovskite solar cells. *Joule* **2**, 1800-1815 (2018).

11. Seo, J. Y. et al. Dopant engineering for Spiro-OMeTAD hole-transporting materials towards efficient perovskite solar cells. *Adv. Funct. Mater.* **31**, 2102124 (2021).

12. Bang, S. et al. Defect-tolerant sodium-based dopant in charge transport layers for highly efficient and stable perovskite solar cells. *ACS Energy Lett.* **5**, 1198-1205 (2020).

13. Seo, J. Y. et al. Novel p-dopant toward highly efficient and stable perovskite solar cells. *Energy Environ. Sci.* **11**, 2985-2992 (2018).

14. Pham, N. D. et al. Alkaline-earth bis(trifluoromethanesulfonimide) additives for efficient and stable perovskite solar cells. *Nano Energy* **69**, 104412 (2020).

15. Luo, J. et al. Molecular doping of a hole-transporting material for efficient and stable perovskite solar cells. *Chem. Mater.* **34**, 1499-1508 (2022).

16. Wu, T. et al. Understanding the effects of fluorine substitution in lithium salt on photovoltaic properties and stability of perovskite solar cells. *ACS Energy Lett.* **6**, 2218-2228 (2021).

17. Gu, X. et al. $FeCl_3$ as a low-cost and efficient p-type dopant of Spiro-OMeTAD for high performance perovskite solar cells. *RSC Advances* **8**, 9409-9413 (2018).

18. Cao, W. et al. Redox engineering of Spiro-OMeTAD based hole transport layer enabled by ultrathin Co(III)-grafted carbon nitride nanosheets for stable perovskite solar cells. *Nano Energy* **104**, 107924 (2022).

19. Wang, X. et al. High performance and stable perovskite solar cells using vanadic oxide as a dopant for Spiro-OMeTAD. *J. Mater. Chem. A* **7**, 13256-13264 (2019).

20. Liu, X. et al. Perovskite solar cells based on Spiro-OMeTAD stabilized with an alkylthiol additive. *Nat. Photonics* **17**, 96-105 (2023).

21. Han, Y. et al. Azide additive acting as a powerful locker for Li^+ and TBP in Spiro-OMeTAD toward highly efficient and stable perovskite solar cells. *Nano Energy* **96**, 107072 (2022).

22. Wu, J. et al. Directly purifiable pre-oxidation of Spiro-OMeTAD for stability enhanced perovskite solar cells with efficiency over 23%. *Chem. Eng. J.* **437**, 135457 (2022).

23. Chen, Q. et al. 3-Chloroperoxybenzoic acid doping Spiro-OMeTAD for improving the performance of perovskite solar cells. *Chem. Eng. J.* **450**, 138313 (2022).

24. Sun, W. et al. Highly efficient and stable planar perovskite solar cells with $K_3[Fe(CN)_6]$-doped Spiro-OMeTAD. *J. Mater. Chem. C* **9**, 7726-7733 (2021).

25. Wan, Z. et al. Chelation of lithium ion with crown ether for eliminating adverse effects caused by Li-TFSI/tBP doping system in Spiro-OMeTAD. *J. Energy Chem.* **74**, 489-496 (2022).

26. Liu, Q. et al. Benzoyl peroxide as an efficient dopant for Spiro-OMeTAD in perovskite solar cells. *ChemSusChem* **10**, 3098-3104 (2017).

27. Shen, Y., Deng, K., Chen, Q., Gao, G. & Li, L. Crowning lithium ions in hole-transport layer toward stable perovskite solar cells. *Adv. Mater.* **34**, 2200978 (2022).

28. Pei, F. et al. Thermal management enables more efficient and stable perovskite solar cells. *ACS Energy Lett.* **6**, 3029-3036 (2021).

29. Yang, Y. et al. Dual functional doping of $KMnO_4$ in Spiro-OMeTAD for highly effective planar perovskite solar cells. *ACS Appl. Energy. Mater.* **2**, 2188-2196 (2019).

30. Yang, H. et al. Iodonium initiators: Paving the air-free oxidation of Spiro-OMeTAD for efficient and stable perovskite solar cells. *Angew. Chem. Int. Ed.* **63**, 202316183 (2024).